Coupled thermohydromechanical analysis of Venice lagoon salt marshes

Simonetta Cola,[1] Lorenzo Sanavia,[2] Paolo Simonini,[1] and Bernhard A. Schrefler[2]

Received 11 October 2007; revised 19 February 2008; accepted 17 March 2008; published 1 August 2008.

[1] A fully coupled thermohydromechanical (THM) finite element approach is used here to model the groundwater and saturation response of a typical salt marsh of the Venice lagoon (Italy) subjected to both tide fluctuation and flooding. The soil forming the marsh, whose relevant material parameters have been measured experimentally in the laboratory, is assumed to be an homogeneous multiphase porous medium, in a thermodynamic equilibrium state both in fully saturated and partially saturated conditions. More particularly, the study is aimed at analyzing separately the various couplings of several factors such as soil stiffness, water conductivity, capillary suction, and humidity exchange with atmosphere including also the occurrence of marsh flooding on the overall mechanical response of the marsh subjected to tidal oscillations of very narrow amplitude. From the analysis carried out so far, the numerical approach adopted here seems capable of describing most of the relevant features of marsh behavior, thus showing the importance of THM couplings to explain the groundwater pressure evolution induced by lagoon tide cycles. In addition, the model seems to provide some interesting explanations concerning the evolving instability of marsh scarps, which is one of the main causes of the rapid overall deterioration of the typical Venice lagoon landscape.

Citation: Cola, S., L. Sanavia, P. Simonini, and B. Schrefler (2008), Coupled thermohydromechanical analysis of Venice lagoon salt marshes, *Water Resour. Res.*, *44*, W00C05, doi:10.1029/2007WR006570.

1. Introduction

[2] The landscape typifying the tidal environment of the Venice lagoon is largely made up of salt marshes and wetlands (Figure 1), largely covered by halophytic vegetation (i.e., adapted to live in salty environment) and subjected to tidal fluctuation, with periods of submersion depending on tidal cycle amplitude and local topography.

[3] The eustatic rise of sea level, natural and/or man-induced regional subsidence, the latter being particularly important between 1946 and 1970 [*Butterfield et al.*, 2003], and the increasing anthropic pressure have caused considerable environmental damage to the lagoon ecosystem, including relevant changes to the sediment balance of the basin and vanishing of large marsh areas. From the beginning of the last century, the whole salt marsh surface has halved and trends would indicate that the marshes should completely disappear over the next 50 years. Moreover, instability of scarps and surface sediment erosion (Figure 2) play key roles in the equilibrium of such delicate environmental system and often require engineered interventions to preserve the existing morphology.

[4] The importance of the Venice lagoon ecosystem stimulated relevant studies on its morphodynamics and evolution as a consequence of various forcing actions [e.g., *Rinaldo et al.*, 1999a, 1999b; *Marani et al.*, 2004, 2007; *Feola et al.*, 2005]. These studies are particularly relevant for the design of any technical intervention for safeguarding such a delicate and unstable environment.

[5] Groundwater response to water fluctuations in tidal environments has been investigated by several researchers [e.g., *Sun*, 1997; *Jiao and Tang*, 1999; *Li et al.*, 2000; *Li and Jiao*, 2002]. Using a finite element approach based on Richard's equation, *Ursino et al.* [2004] showed recently the great relevance of the unsaturated subsurface groundwater regime with respect to the growth of halophytic vegetation in areas cyclically subjected to tidal inundation, such as in the Venice lagoon salt marshes.

[6] The present paper enhances a previous attempt by *Cola et al.* [2005] to model the groundwater and saturation response of a typical lagoon marsh subjected to both tide fluctuation and inundation by using a coupled thermohydromechanical (THM) model.

[7] The soil forming the salt marsh is assumed to be a multiphase porous medium, in a thermodynamic equilibrium state in fully saturated and partially saturated conditions. The multiphase material is modeled as a deforming porous continuum where heat, water, and gas flow are taken into account [*Gawin and Schrefler*, 1996; *Lewis and Schrefler*, 1998]. Particularly, the gas phase is modeled as an ideal gas composed of dry air and water vapor, which are considered as two miscible species. Phase changes of water (evaporation-condensation, adsorption-desorption) and heat transfer through conduction and convection, as well as latent heat transfer are considered. The independent variables are the

[1]Department of Hydraulic Engineering, Maritime, Environmental, and Geotechnics, University of Padova, Padua, Italy.
[2]Department of Structural and Transportations Engineering, University of Padova, Padua, Italy.

0043-1397/08/2007WR006570$09.00

Figure 1. View of the Venice lagoon marshes.

solid displacements, capillary pressure, gas pressure, and temperature. Small strains and quasi-static loading conditions are assumed.

[8] To characterize marsh soils as carefully as possible in order to evaluate the model parameters, geotechnical investigations have been concentrated in a typical lagoon marsh area, with soil profile reconstruction, permeability and compressibility measurements in both saturated and unsaturated condition. In the same area the tide-induced water pressure evolution in the upper layers of the marsh was monitored by using some special piezometers.

[9] This paper presents the results of numerical analysis showing the relevance of coupling effects on the overall saturated and unsaturated groundwater response of the salt marsh subjected to both tide fluctuation and inundation. Evapotranspiration of the marsh surface has also been simulated. This phenomenon requires evaporation of the water to be taken into account in the multiphase model, for which a nonisothermal formulation is needed, as proposed in the paper. Influence on the distribution of stress field on the long-term stability of marsh scarp is also discussed.

2. Properties of the Venice Lagoon Soils

[10] The plain surrounding the Venice lagoon was formed throughout the Pleistocene as a consequence of fluvial transport of sediments coming from the erosion of the surrounding Alps. The lagoon origin is traced around 6000 years ago, during the Flandrian transgression, with the seawater diffusing into a preexisting lacustrine basin. Both continental and marine sediments therefore coexist in the lagoon area with the typical ground profiles being the consequence of such a complex geological history.

[11] The first Venetian citizens, settled on the main islands inside the lagoon around XII century subjected this

Figure 2. View of Saint Felice marsh border.

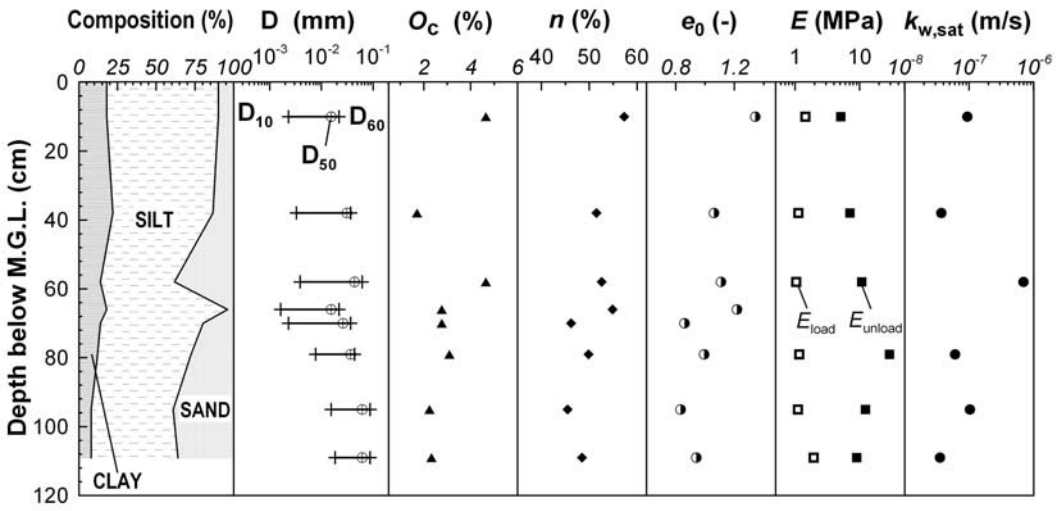

Figure 3. Basic properties of shallow soils and permeability profile along vertical SF2.

unequaled geological site to an intensive human action, mostly concerned with sediment dredging and land filling in order to conserve efficient communications both inside the lagoon basin and with the open sea.

[12] The sediments forming the whole Venice lagoon basin share a common geological origin and similar depositional environments, resulting in a narrowly varying mineralogical composition. In terms of particle size, a predominant silt fraction is mostly combined with clay and/or sand in a chaotic interbedding and interdigitation of different sediments: typical soil profiles are therefore characterized by highly heterogeneous layering of mixes of sand, silt, and clay-sized soil particles with the presence, in some cases, of shell content and thin peaty layers.

[13] Comprehensive geomechanical characterization of such heterogeneous and complex materials has been recently carried out by *Cola and Simonini* [2002], *Simonini* [2004], *Simonini et al.* [2007], and *Biscontin et al.* [2007]. More particularly, from experimental investigation carried out so far it turned out that the mechanical soil behavior can be described in terms of frictional (typical of coarse-grained fraction) rather than of electrochemical (typical of fine-grained fraction) interaction among the sediments, with the exception of a very few cases of more plastic clays [*Cola and Simonini*, 2002].

3. Salt Marsh Geotechnical Characterization and Constitutive Equations

[14] The marsh selected for the experimental investigation and in situ monitoring is located on the north side of the Saint Felice channel.

[15] In order to characterize, as carefully as possible, soils forming the upper part of the marsh (about the first meter from the ground level), undisturbed samples were manually collected. Then, laboratory tests were carried out in order to determine the grain size distribution, natural water content (w_o), organic content (O_C), in situ density (γ), porosity (n) and in situ void ratio (e_o) and to reconstruct profiles of these properties as precisely as possible.

[16] Figure 3 depicts soil profile and the main basic indices of the soils. As already mentioned, the soils are a mixture of sand, silt and clay (see first column) with a predominant silty fraction (about 60–70%) and a small content of clay (the fraction with diameter smaller then 2 μm is about 10–18%). The mean diameter D_{50} is around 0.03 mm, while the 10% of material has diameters less then 0.003 mm (see column 2). The organic material, composed of residuals of small root and plant fragments, varies between 2 and 8% of the dry weight of the soil (column 3). Porosity and void ratio (columns 4 and 5) are relatively high compared with the typical values of the deeper soils, and their variations are conditioned by the organic content: a small increase of the O_C, observed especially in the shallowest 15 cm of the profile, gives increments of about 50% of the void ratio.

[17] Figure 3 summarizes some experimental values of the stiffness E and saturated hydraulic conductivity $k_{w,sat}$. Because of the small stress range induced by tidal forcing and no evident material damage, a linear elastic material model will be used to describe the soil skeleton response in the numerical analyses:

$$d\boldsymbol{\sigma}' = \frac{E}{1+\nu} d\boldsymbol{\varepsilon} + \frac{E\nu}{(1+\nu)(1-2\nu)} (d\boldsymbol{\varepsilon} : \mathbf{1})\mathbf{1} \qquad (1)$$

where $\boldsymbol{\sigma}'$ is the modified Cauchy effective stress tensor, also called generalized Bishop stress tensor [*Nuth and Laloui*, 2008], ε is the small strain tensor and $\mathbf{1}$ is the second-order identity tensor. Young modulus E and Poisson ratio ν are material parameters.

[18] The values of stiffness E reported in Figure 3 were estimated from one-dimensional compression tests at a stress level corresponding to the site overburden stress, in both loading (E_{load}) and unloading (E_{unload}) conditions. As it is evident in Figure 4, in which a typical 1-D compression curve for the marsh soils is depicted, a great difference in stiffness values measured in loading and unloading condition, being the first 1 order of magnitude smaller (1.0 to 1.5 MPa) than the second (5.0 to 25.0 MPa). Poisson ratio was assumed $\nu = 0.20$, which is a typical small-strain value for Venetian materials according to *Cola and Simonini* [1999].

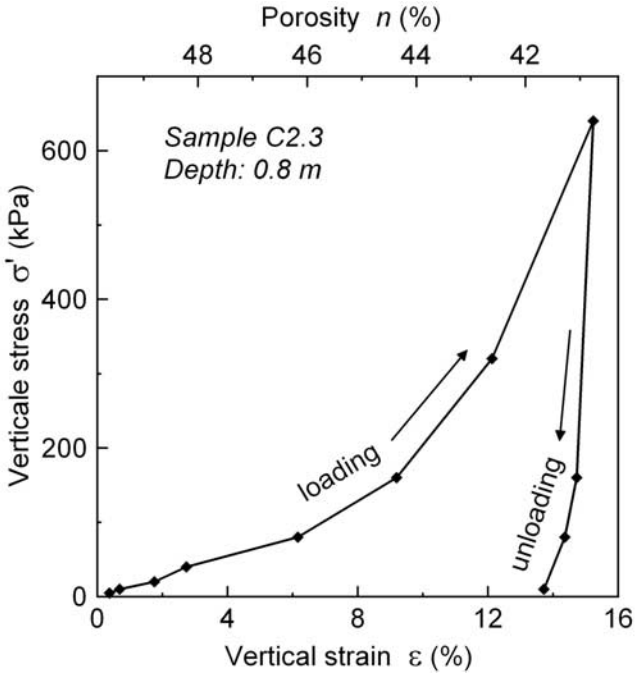

Figure 4. Typical one-dimensional compression response.

[19] The experimental retention curve of a typical shallow clayey silt sample [*Ceron*, 2005], determined using the mercury intrusion porosimeter technique developed by *Romero et al.* [1999], is shown in Figure 5. To note that mercury porosimeter allows to measure reliable suction pressures at low water saturation degrees (S_w), whereas approaching $S_w = 1$, where suction pressure vanishes, experimental data conflicts with the expected response of soil. Therefore, in order to exclude unreasonable material behavior approaching $S_w = 1$, the measured trend has been fitted by the equation (plotted in Figure 5)

$$S_w = 1 - 0.344\left(\frac{p^c}{p_a}\right)^{0.845} \tag{2}$$

being p^c the suction or capillary pressure ($p_a = 100$ kPa).

[20] Water conductivity $k_{w,sat}$, determined on saturated samples using falling head tests in oedometer cell at

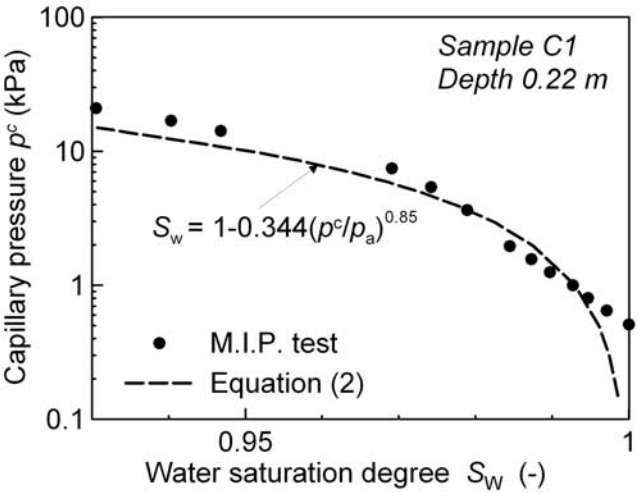

Figure 5. Experimental and analytical retention curves.

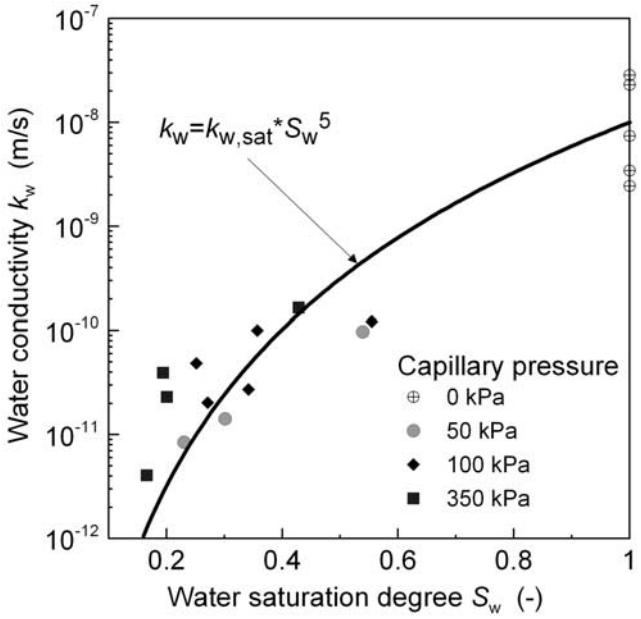

Figure 6. Water conductivity from tests and analytical relationship.

overburden effective stress, lies between 3×10^{-8} m/s and 9×10^{-7} m/s. The effect of partial saturation on water conductivity k_w, investigated in the full range of saturation, was measured on a typical soil sample, over a large range of vertical effective stress in isothermal condition, by means of a special laboratory odometer cell developed for testing unsaturated soils [*Ceron*, 2005]. Note that at full saturation, the soil conductivity decreases from 3×10^{-8} m/s to 2×10^{-9} m/s as according to the decrease of porosity induced by the increasing applied mean effective stress.

[21] It is important to notice the significant effect of saturation on k_w, even for small variation of S_w. The equation fitting the experimental data, sketched in the Figure 6, is

$$k_w = k_{w,sat}(S_w)^5 \tag{3}$$

In absence of direct measurements of gas conductivity, the relationship of *Brooks and Corey* [1966] in isothermal condition has been selected for the evaluation of the gas relative permeability $k^{rg}(S_w)$ (see equations (10) and (11)).

[22] The gas phase in the soil is a mixture of dry air and water vapor, both assuming to behave as ideal gases. According to the equation of the state of perfect gas (the Clapeyron equation) and Dalton's law, the pressure of dry air p^{ga} with density ρ^{ga}, water vapor p^{gw} with density ρ^{gw}, and moist air p^g with density ρ^g are

$$p^{ga} = \rho^{ga}RT/M_a \qquad p^{gw} = \rho^{gw}RT/M_w \tag{4}$$

$$p^g = p^{ga} + p^{gw} \qquad \rho^g = \rho^{ga} + \rho^{gw} \tag{5}$$

where M_a and M_w are the molar mass of dry air and of water, respectively, and T is the temperature.

[23] In the partially saturated zones, the equilibrium water vapor pressure p^{gw} is obtained from the Kelvin-Laplace equation

$$p^{gw} = p^{gws}(T)\exp\left(-\frac{p^c M_w}{\rho^w RT}\right) \tag{6}$$

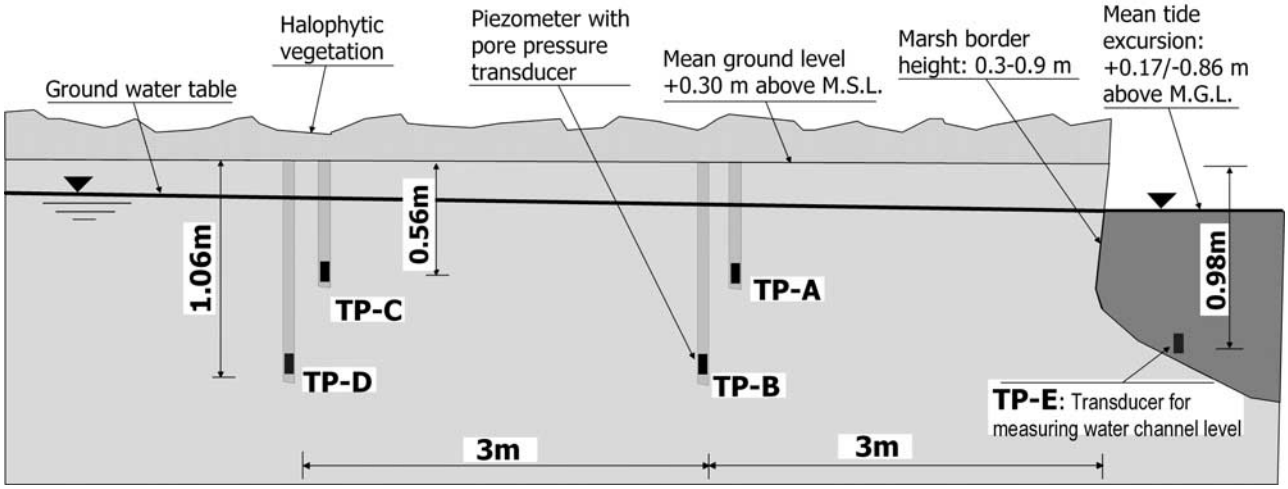

Figure 7. Layout of pore pressure transducers at the marsh border.

where the water vapor saturation pressure p^{gws}, depending only upon the temperature, is calculated from the Clausius-Clapeyron equation.

4. In Situ Water Pressure Measurements

[24] Figure 7 sketches a schematic layout of the pore pressure measurement system installed into the ground at the Saint Felice marsh [*Simonini and Cola*, 2002]. The water pressure was monitored at two depths, namely, at 0.56 m and 1.06 m below the mean marsh ground level (MGL), and at distance of 3 m and 6 m from the marsh border.

[25] Standpipe piezometers were provided by a special water pressure transducer, equipped with a remote recording system. An additional water pressure transducer measured the tide oscillation in the nearby channel.

[26] Water pressure was continuously measured for some months during 2002 and then transformed in total head referred to the mean marsh ground level assumed at +0.30 m above the mean sea level (MSL).

[27] Figure 8 shows a typical tidal cycle for a 14-day-long interval. The tidal fluctuation, not constant over the monitoring period, submerges the marsh only in a few of episodes whose duration does not exceed some hours. Note also the occurrence of relatively long intervals during which the tide remains below the marsh surface.

[28] In order to depict the typical marsh hydraulic response in different submersion/no-submersion conditions, only a portion of the semicycle of Figure 8, i.e., the interval 7 days long from 13 to 20 March 2002, is proposed again in Figures 9 and 10 and compared with the total head evolution measured in the ground over at two different distances from the marsh border, namely, at 3.0 and 6.0 m. It is worthwhile to notice that at the submersion occurrence, the water table in the ground suddenly increases as a consequence of a vertical water flow, highlighted by the two different water levels measured in the transducers located along with the same vertical. On the contrary, at negative tidal fluctuation, the water pressure shows a significant delay and damping remaining the water pressure always positive up to a depth about 0.30 m below MGL, even for tides approaching −0.80 m. In addition, it is interesting to notice that, in no-submersion long periods (i.e., from 9th to 12th day in Figures 9 and 10), the oscillating water table gradually decreases according to the tidal fluctuation in the nearby channel. On the base of the piezometer

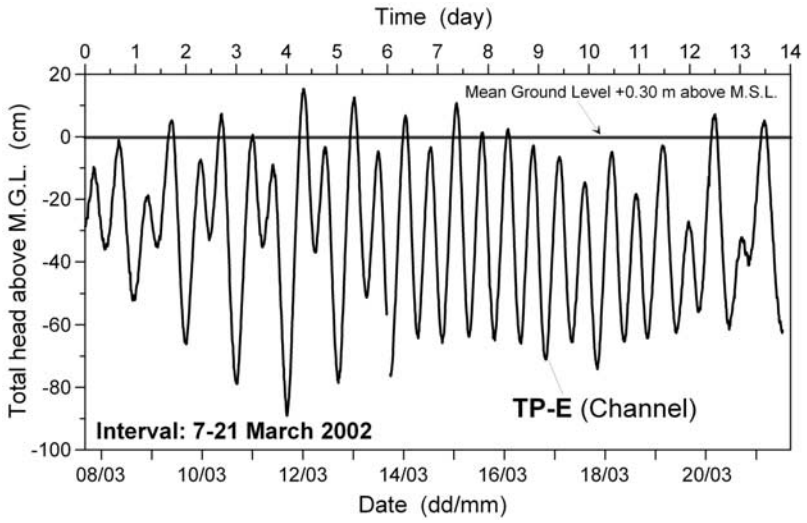

Figure 8. Tide level in the channel monitored by TP-E in the period 7−21 March 2002.

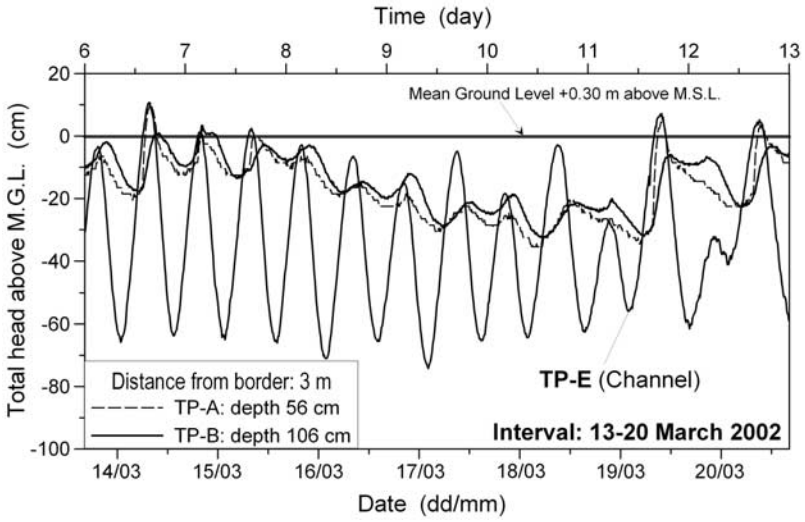

Figure 9. Tide level in the channel compared with total head monitored by TP-A and TP-B in 7-day interval.

readings, showing the permanence of a shallower water table in the inner zone of the marsh, ground dewatering seems to be controlled mainly by the horizontal flow. Evapotranspiration may cause an additional flow in vertical direction. However, this is not so clearly appreciable from site readings carried out in March, which is characterized by low humidity and temperature gradients in the Venice lagoon.

[29] It is important to note that the water pressure evolution discussed above is due to a selected short time interval, being the usual water pressure trend in the range ±0.60 m above MSL, with the oscillation amplitude typically controlled by the 28-day moon cycle. Under very low atmospheric pressure and blowing southeast wind, tide may exceptionally rise above 1.0 m above MSL.

5. Mathematical and Numerical Model

[30] The thermohydromechanical behavior of the marshes is modeled using a coupled finite element model for non-isothermal multiphase materials [*Gawin and Schrefler*, 1996; *Lewis and Schrefler*, 1998; *Sanavia et al.*, 2006]. This model derives from the mathematical model developed by *Lewis and Schrefler* [1998] and *Schrefler* [2002] using averaging theories by *Hassanizadeh and Gray* [1979a, 1979b, 1980].

[31] In this model, the porous medium is treated as multiphase system composed of a solid skeleton (s) and open pores filled with water (w) and gas (g) (in partially saturated conditions) or only with water (in saturated conditions). The gas is assumed to behave as an ideal mixture of two species: dry air (noncondensable gas, ga) and water vapor (condensable one, gw).

[32] At the macroscopic level the porous media material is modeled as a deformable continuum in which constituent has a reduced density according to its volume fraction. The constituents are assumed to be isotropic, homogeneous, chemically nonreacting and immiscible, with the exception

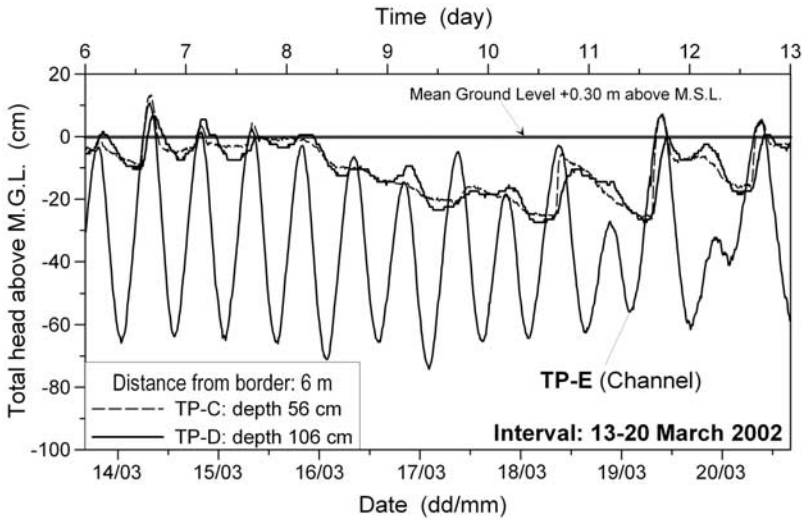

Figure 10. Tide level in the channel compared with total head monitored by TP-C and TP-D in 7-day interval.

of the latter for dry air and vapor. At micro level, the porous medium is constituted of incompressible solid and water constituents. Several phenomena are taken into account including water flow due to pressures gradients, heat conduction and convection, vapor diffusion and latent heat transfer, as a result of the phase exchange of water inside the pores.

[33] Fluids, solid and thermal fields are coupled; the fluids are in contact with the solid. All the constituents are taken to have the same temperature because the local thermal equilibrium between solid, gas and liquid phases is assumed.

[34] The state of the medium is described by capillary pressure $p^c(\boldsymbol{x}, t)$, gas pressure $p^g(\boldsymbol{x}, t)$, temperature $T(\boldsymbol{x}, t)$ and displacements of the solid matrix $\boldsymbol{u}(\boldsymbol{x}, t)$, where $\boldsymbol{x}$ is the vector of the spatial coordinates and t is the current time (for a detailed discussion about the chosen primary variables, see *Sanavia et al.* [2006]). In the partially saturated zones water is separated from its vapor by a concave meniscus (capillary water). Because of the curvature of this meniscus the sorption equilibrium equation gives the relationship among the capillary pressure $p^c(\boldsymbol{x}, t)$ and the gas and water pressure, $p^g(\boldsymbol{x}, t)$ and $p^w(\boldsymbol{x}, t)$, respectively,

$$p^c = p^g - p^w \tag{7}$$

Water pressure is defined as compressive positive for the fluids, while stress is defined as tension positive for the solid phase.

[35] Moreover, as usual in multiphase materials theory, the motion of the fluids is described in terms of motion relative to the solid. This means that a fluid relative velocity with respect to the solid $\boldsymbol{v}^{\pi s} = \boldsymbol{v}^{\pi} - \boldsymbol{v}^{s}$, with $\pi = g, w$ is introduced.

[36] The four balance equations of the model are summarized in the following. The linear momentum balance equation of the mixture in terms of total Cauchy stress $\boldsymbol{\sigma}(\boldsymbol{x}, t)$ assumes the form

$$\mathrm{div}\ \boldsymbol{\sigma} + \rho\mathbf{g} = \mathbf{0} \tag{8}$$

where ρ is the density of the mixture $\rho = [1 - n]\rho^s + nS_w\rho^w + nS_g\rho^g$, with $n(\boldsymbol{x}, t)$ the porosity and $S_w(\boldsymbol{x}, t)$ and $S_g(\boldsymbol{x}, t)$ the water and gas degree of saturation, respectively ($S_w + S_g = 1$); $\mathbf{g}$ is the gravity acceleration vector.

[37] The total Cauchy stress is decomposed into the effective and pressure (equilibrium) parts following the principle of effective stress:

$$\boldsymbol{\sigma} = \boldsymbol{\sigma}' - \lfloor S_g p^g + S_w p^w \rfloor \mathbf{1} = \boldsymbol{\sigma}' - \lfloor p^g - S_w p^c \rfloor \mathbf{1} \tag{9}$$

This generalization of the Bishop stress [*Nuth and Laloui*, 2008] using saturation as weighting functions for the partial pressures was introduced by *Schrefler* [1984] using volume averaging for the bulk materials and is thermodynamically consistent [*Gray and Hassanizadeh*, 1991; *Gray and Schrefler*, 2001] (and recently also *Borja* [2004]). On the contrary, *Gray and Schrefler* [2001] showed that the Bishop parameters, area fraction, instead of saturations as weighting factors [*Bishop and Blight*, 1963] are not thermodynamically consistent without additional terms (see *Schrefler* [2002] as well). This equation was also derived from continuum thermodynamics by *Hutter et al.* [1999] using mixture theory by *Ehlers et al.* [2004] within the framework of the theory of porous media and by *Coussy* [2007] in case of isodeformation assumption and porous media with disconnected networks using a Lagrangian saturation concept.

[38] The decomposition of equation (9) permits a straightforward transition between saturated and partially saturated conditions. Moreover, it enables to take into account the direct change in the effective stress by any increase in capillary pressure and enables a natural repercussion of the hydraulic hysteresis observed in $(S_w - p^c)$ plane into $(p^c - p')$ representation [*Nuth and Laloui*, 2008], where p' is the mean effective pressure.

[39] The mass conservation equation for the solid skeleton, the water and the vapor is

$$\begin{aligned} &n[\rho^w - \rho^{gw}]\frac{\partial S_w}{\partial t} + \left[\rho^w S_w - \rho^{gw} S_g\right]\mathrm{div}\left(\frac{\partial \mathbf{u}}{\partial t}\right) + nS_g\frac{\partial \rho^{gw}}{\partial t} \\ &\quad - \mathrm{div}\left(\rho^g \frac{M_a M_w}{M_g^2}\mathbf{D}_g^{gw}\,\mathrm{grad}\left(\frac{p^{gw}}{p^g}\right)\right) \\ &\quad - \mathrm{div}\left(\rho^w \frac{\mathbf{k}k^{rw}}{\mu^w}\left[\mathrm{grad}(p^w) - \rho^w\mathbf{g}\right]\right) \\ &\quad - div\left(\rho^{gw}\frac{\mathbf{k}k^{rg}}{\mu^g}\left[\mathrm{grad}(p^g) - \rho^g\mathbf{g}\right]\right) - \beta_{swg}\frac{\partial T}{\partial t} = 0 \end{aligned} \tag{10}$$

where $\boldsymbol{k}(\boldsymbol{x}, t) = k(\boldsymbol{x}, t)\mathbf{1}$ is the intrinsic permeability tensor [L^2], $k^{rw}(\boldsymbol{x}, t)$ is the water relative permeability parameter, and $\mu^{\pi}(\boldsymbol{x}, t)$ is the fluid viscosity ($\pi = w, g$). $\mathbf{D}_g^{gw}(\boldsymbol{x}, t) = D_g^{gw}\ \mathbf{1}$ means the effective diffusivity tensor of water vapor in dry air and $M_g(\boldsymbol{x}, t)$ is the molar mass of gas mixture. $\beta_{swg}(\boldsymbol{x}, t)$ combines the solid-liquid cubic thermal expansion coefficients ($\beta_{swg} = [1 - n]\beta_s[S_g\rho^{gw} + \rho^w S_w] + n\beta_w\rho^w S_w$).

[40] Similarly, the mass balance equation for the dry air is

$$\begin{aligned} &-n\rho^{ga}\frac{\partial S_w}{\partial t} + \rho^{ga}S_g\mathrm{div}\left(\frac{\partial \mathbf{u}}{\partial t}\right) + nS_g\frac{\partial \rho^{ga}}{\partial t} \\ &\quad - \mathrm{div}\left(\rho^g\frac{M_a M_w}{M_g^2}\mathbf{D}_g^{ga}\,\mathrm{grad}\left(\frac{p^{ga}}{p^g}\right)\right) \\ &\quad - \mathrm{div}\left(\rho^{ga}\frac{\mathbf{k}k^{rg}}{\mu^g}\left[\mathrm{grad}(p^g) - \rho^g\mathbf{g}\right]\right) \\ &\quad - \beta_s\rho^{ga}[1 - n]S_g\frac{\partial T}{\partial t} = 0 \end{aligned} \tag{11}$$

where $\mathbf{D}_g^{ga}(\boldsymbol{x}, t) = \mathrm{D}_g^{ga}\ \mathbf{1}$ is the effective diffusivity tensor of dry air in water vapor. The quantities $S_w(\boldsymbol{x}, t)$, $S_g(\boldsymbol{x}, t)$, $k^{rw}(\boldsymbol{x}, t)$, and $k^{rg}(\boldsymbol{x}, t)$ are defined at the constitutive level, as described in section 3. Both inflow and outflow in equations (10) and (11) have been described using the Fick law for the diffusion of the vapor in the gas phase and by the Darcy law for the water and the gas flows.

[41] The energy balance equation of the mixture is

$$\begin{aligned} &\left(\rho C_p\right)_{eff}\frac{\partial T}{\partial t} + \rho^w C_p^w\left[\frac{\mathbf{k}k^{rw}}{\mu^w}\left[-\mathrm{grad}(p^g) + \mathrm{grad}(p^c) + \rho^w\mathbf{g}\right]\right]\mathrm{grad}(T) \\ &\quad - \mathrm{div}\left(\chi_{eff}\,\mathrm{grad}(T)\right) - \rho^g C_p^g\left[\frac{\mathbf{k}k^{rg}}{\mu^g}\left[\mathrm{grad}(p^g) - \rho^g\mathbf{g}\right]\right] \\ &\quad \cdot\,\mathrm{grad}(T) = -\dot{m}_{vap}\Delta H_{vap} \end{aligned} \tag{12}$$

where $(\rho C_p)_{eff}(\boldsymbol{x}, t)$ is the effective thermal capacity of porous medium, $C_p^w(\boldsymbol{x}, t)$ and $C_p^g(\boldsymbol{x}, t)$ are the specific heat of water and gas mixture, respectively, and $\chi_{eff}(\boldsymbol{x}, t)$ is the effective thermal conductivity of the porous medium. The right-hand side term $\dot{m}_{vap}\ \Delta H_{vap}$ considers the contribution of the evaporation and condensation. This balance equation takes into account the heat transfer through conduction and

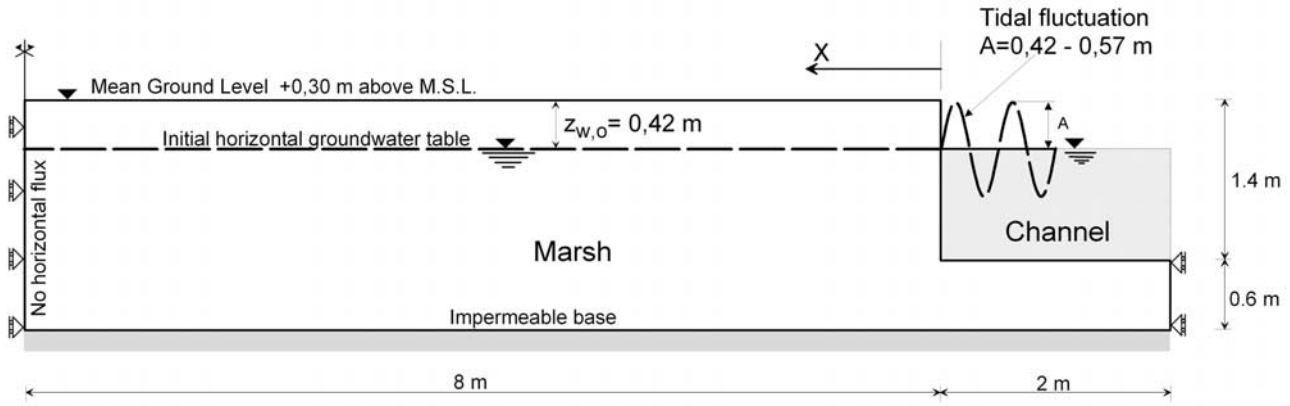

Figure 11. Bidimensional scheme of marsh used in numerical analysis.

convection as well as latent heat transfer [see *Gawin and Schrefler*, 1996; *Lewis and Schrefler*, 1998] and neglects the terms related to the mechanical work induced by density variations due to temperature changes of the phases and induced by volume fraction changes. The interested reader can find a new model including the effects of the air dissolved in water in the work by *Gawin and Sanavia* [2008].

[42] The model of equations (8)–(12) recovers that of *Biot* [1941] assuming water saturated material under isothermal conditions. Moreover, using Biot's phenomenological approach, it is possible to derive the model of this work extending the one of Biot by including nonisothermal and partially saturated conditions [see *Lewis and Schrefler*, 1998, section 2.6].

[43] The initial conditions for the full fields of primary state variables at the reference time $t = t_0$ in the whole domain (B) and on its boundary (∂B) are defined as

$$p^g = p_0^g,\ p_c = p_0^c,\ T = T_0,\ \mathbf{u} = \mathbf{u}_0,\ \text{on},\ B \cup \partial B.$$

[44] The boundary conditions (BCs) are of Dirichlet's type on $\partial B\pi$ for $t \geq t_0$:

$$p^g = \hat{p}^g \text{ on } \partial B_g, \quad p^c = \hat{p}^c \text{ on } \partial B_c,$$
$$T = \hat{T} \text{ on } \partial B_T, \quad \mathbf{u} = \hat{\mathbf{u}} \text{ on } \partial B_u \tag{13}$$

or of Cauchy BCs type on $\partial B^q\pi$ for $t \geq t_0$:

$$\begin{aligned}
&(\rho^{ga}\mathbf{v}^g - \rho^g\mathbf{v}^{gw}) \cdot \mathbf{n} = q^{ga} \text{ on } \partial B_g^q,\\
&(\rho^{gw}\mathbf{v}^g + \rho^w\mathbf{v}^w + \rho^g\mathbf{v}^{gw}) \cdot \mathbf{n} = \beta_c\left(\rho^{gw} - \rho_\infty^{gw}\right) + q^{gw} + q^w \text{ on } \partial B_c^q,\\
&-\left(\rho^w\mathbf{v}^w\Delta h_{vap} - \lambda_{eff}\nabla T\right) \cdot \mathbf{n} = \alpha_c(T - T_\infty) + q^T \text{ on } \partial B_T^q,\\
&\boldsymbol{\sigma} \cdot \mathbf{n} = \mathbf{t} \text{ on } \partial B_u^q,
\end{aligned} \tag{14}$$

where $\mathbf{n}(\boldsymbol{x}, t)$ is the unit normal vector, pointing toward the surrounding gas, $q^{ga}(\boldsymbol{x},t)$, $q^{gw}(\boldsymbol{x},t)$, $q^w(\boldsymbol{x},t)$, and $q^T(\boldsymbol{x},t)$ are the imposed fluxes of dry air, vapor, liquid water, and the imposed heat flux, respectively, and $\mathbf{t}(\boldsymbol{x}, t)$ is the imposed traction vector related to the total Cauchy stress tensor $\boldsymbol{\sigma}(\boldsymbol{x},t)$; $\rho_\infty^{gw}(\boldsymbol{x},t)$ and $T_\infty(\boldsymbol{x},t)$ are the mass concentration of water vapor and the temperature in the far field of undisturbed gas phase, while $\alpha_c(\boldsymbol{x},t)$ and $\beta_c(\boldsymbol{x},t)$ are convective heat and mass exchange coefficients.

[45] As pointed out in section 3, the mechanical behavior of the solid skeleton is assumed to be linear elastic. For the interested reader, the elastoplastic formulation is developed by *Sanavia et al.* [2006] within the classical elastoplasticity theory for geometrically linear problems, where the return mapping and the consistent tangent operator is derived for the Drucker-Prager model in isothermal conditions for isotropic linear hardening/softening and volumetric-deviatoric non-associative plasticity (the formulation for geometrically nonlinear problems is developed in the work of *Sanavia et al.* [2002]). Moreover, a nonisothermal elastoplastic model is proposed by *Sanavia et al.* [2008], following the work by *Laloui and Cekerevac* [2003] and *Laloui et al.* [2005].

[46] In the finite element formulation, the balance equations (8), (10)–(12) are discretized in space and time by using the finite element method for coupled problems, as described, e.g., by *Lewis and Schrefler* [1998] or *Zienkiewicz et al.* [1999].

[47] In particular, after spatial discretization by applying the Galerkin procedure within the isoparametric formulation, a nonsymmetric, nonlinear and coupled system of semi-discretized equation is obtained. After time integration by the generalized trapezoidal method, the nonlinear system of algebraic equation is linearized, thus obtaining the linear equations system that can be solved numerically.

[48] Details concerning the matrices and the residuum vectors of the linearized equations system can be found in the work of *Sanavia et al.* [2006]. Owing to the strong coupling between the mechanical and the pore fluid problem, a monolithic solution is preferred using a Newton scheme [*Bianco et al.*, 2003].

[49] The Galerkin procedure has been selected for the numerical solution of the governing equations even in presence of convective terms in the energy balance equation of the mixture (12) to solve slow phenomena, in which the convective terms remain small as compared to the diffusion term [see, e.g., *Zienkiewicz and Taylor*, 2000a, section 3.12.3] for the case of convective-diffusion equations). This is also confirmed by the computed Peclet number [see, e.g., *Zienkiewicz and Taylor*, 2000b, section 2.2], which is proportional to the ratio between the convective velocity and the diffusion term, thus turning out very small for the cases analyzed here.

6. Domain Geometry, Initial and Boundary Conditions of the Marsh

[50] The Saint Felice marsh is a relatively narrow peninsula, laterally confined by two streams. Taking into account

its relevant geometrical ratios and the symmetry of problem, the Saint Felice marsh was modeled as a two-dimensional domain, as shown in Figure 11.

[51] The spatial domain is discretized with eight-node Serendipity finite elements of equal size for the solid displacements, temperature, gas pressure and capillary pressure. Full numerical integration is selected. This element violates the LBB condition (or the equivalent patch test for mixed formulations [*Zienkiewicz and Taylor*, 2000a]), but convergence, consistency, and stability of the numerical solution are guaranteed because the undrained limit state due to very small permeability is never approached [see, e.g., *Lewis and Schrefler*, 1998]. Moreover, the numerical solution is accurate, in the sense that the phenomenon analyzed in this work is essentially a consolidation problem that can be solved exactly, according to our experience, using this type of element for both mean effective stress and water pressure.

[52] The soil forming the marsh is assumed to be an homogeneous, isotropic material, characterized by specific gravity of soil particles equal to 2.7 and by porosity of 44%.

[53] To investigate the influence of soil stiffness on the coupled behavior, two reasonable soil skeleton stiffness were selected for the analyses, namely, E = 1.2 MPa and E = 12 MPa, which are typical values in loading and unloading condition. Moreover, to evaluate the effect of a further increase of soil stiffness, an elastic modulus E = 120 MPa (i.e., very rigid soil skeleton compared to the induced stress levels) was also used.

[54] The effect of water conductivity was analyzed assuming two values of $k_{w,sat}$, representing the lower and upper limit of the experimental data range, i.e., $k_{w,sat} = 10^{-6}$ m/s and $k_{w,sat} = 10^{-8}$ m/s. Other relevant parameters have been selected according to the constitutive equations described in section 3.

[55] The numerical model requires the initial distribution of stresses, capillary and gas pressures and temperature in equilibrium with the thermohydraulic boundary conditions. These initial distributions were obtained by performing a preanalysis with uniform gas pressure (equal to the atmospheric pressure) and with water pressure according to a horizontal water table at 0.42 m below MGL and taking into account the gravity forces.

[56] In order to evaluate the effect of stiffness and water conductivity on the overall marsh behavior, a first group of numerical tests were carried out applying a sinusoidal forcing cycle, composed of two semidaily ±0.42 m amplitude oscillations, thus reproducing a lagoon tide not submerging the marsh.

[57] A second group of tests was then performed to investigate the influence of marsh flooding, by increasing the amplitude of the forcing tide up to ±0.57 m.

[58] Third, in order to investigate the behavior over a longer period, in which a typical full inundation is followed by some days of nonsubmersion, additional numerical analyses have been performed. These have run over a whole of 96 h (4 days) composed by first 24 h of inundating tidal cycles and 72 subsequent hours of nonsubmerging cycles.

[59] Finally, to evaluate the possible influence of evapotranspiration, an additional analysis was performed by imposing a relative humidity of 75% to the undisturbed gas phase in contact with the mash surface; this value is kept constant throughout the simulation over 96 h.

[60] Table 1 summarizes the range of variation of parameters and/or relevant boundary conditions.

[61] It is important to point out that the numerical simulations carried out so far use as forcing action a simple sinusoidal tide, which is different from the measured water table excursion depicted in Figures 9 and 10. This choice is particularly aimed, in this context, at analyzing separately the various couplings of several factors such as soil stiffness, water conductivity, capillary suction, humidity exchange with atmosphere including also the occurrence of marsh flooding, on the overall mechanical response of the marsh, discussing the role of experimentally measured soil parameters and of the relevant boundary conditions. For a simulation of the measured water table excursion, now possible on the basis of the performed model calibration, other important factors such as air temperature and rainfall require additional experimental measurements to be included into a fully coupled analysis, that has been already planned as future development of the research.

7. Numerical Results: Water Pressure and Saturation Oscillations

7.1. Influence of Water Conductivity and Soil Stiffness

[62] In order to investigate the influence of relative water conductivity and to calibrate overall marsh response to groundwater seepage, two first numerical analyses were carried out with $k_{w,sat} = 10^{-6}$ m/s and $k_{w,sat} = 10^{-8}$ m/s and an unique value of soil stiffness, namely, E = 12 MPa.

[63] Figure 12 sketches the evolution of water pressure (expressed in terms of total head) and saturation degree at two significant points (A and B), located at the same depth of 0.42 m below MGL and at increasing distance of x = 1.0 m and x = 3.0 m from the marsh outer border. Figure 13 displays the results obtained in the analyses at constant conductivity ($k_{w,sat} = 10^{-6}$ m/s) but variable soil stiffness (E = 1.2, 12 and 120 MPa), again evaluated at points A and B.

[64] From these results some interesting observations can be drawn:

[65] 1. With higher water conductivity, the steadily symmetrical water pressure oscillation in the ground shows relevant damping and delay with respect to the external forcing cycle. On the contrary, with smaller conductivity, the marsh appears to behave as impermeable, being the free water surface already stable at both points A and B, irrespective of the distance from marsh border. In this case the marsh remains, at that depth, fully saturated throughout the tidal cycle.

[66] 2. The oscillation amplitude calculated at point B in the case of higher conductivity seems to properly approach the field measurements depicted in Figure 9. This result appears to support the hypothesis that higher conductivity characterizes the marsh soil at larger scale, even though smaller values were measured in laboratory. These apparently conflicting aspects may be justified considering that the natural Venetian sediments are highly interstratified with the presence of thin sand or silty sand laminations, effecting an overall increase of permeability in horizontal

Table 1. Relevant Soil Properties and Boundary Conditions

Soil Parameter or Boundary Condition	Selected Values	Comment
Soil elastic stiffness (MPa)	1.2	Loading stiffness
	12	Unloading stiffness
	120	Almost rigid
Water conductivity in saturated condition (m/s)	10^{-6}	Maximum
	10^{-8}	Minimum
Tidal oscillation (m)	±0.42	Marsh not submerged
	±0.57	Marsh flooded
Duration of simulation (h)	24	Not submerged
	96	24 h flooding tidal cycles followed by 72 h of nonsubmerging cycles
Humidity exchange with atmosphere	Yes/No	24 h flooding tidal cycles followed by 72 h of nonsubmerging cycles

direction [*Cola and Simonini*, 2002]. On the basis of such considerations, $k_{w,sat} = 10^{-6}$ m/s is assumed, in this context, to govern the seepage flow in all the following numerical analyses.

[67] 3. The two extreme values of stiffness measured in laboratory, i.e., E = 1.2 MPa and E = 12.0 MPa, provide significant differences in groundwater and saturation regime, at both points A and B. In addition, it is interesting to note that any further stiffness increase (E = 120 MPa) does not produce any appreciable variation in the total head oscillation. Comparing the numerical simulations with site groundwater measurements, it is possible to point out that the real soil stiffness may probably lie in the range between the two values assumed here, thus confirming the effectiveness of the selected elastic moduli.

[68] 4. The S_w oscillation follows the water pressure response. With $k_{w,sat} = 10^{-6}$ m/s, the vadose zone expands in accordance with the negative water fluctuation, reaching the smallest value of 0.95 at the ground surface. During

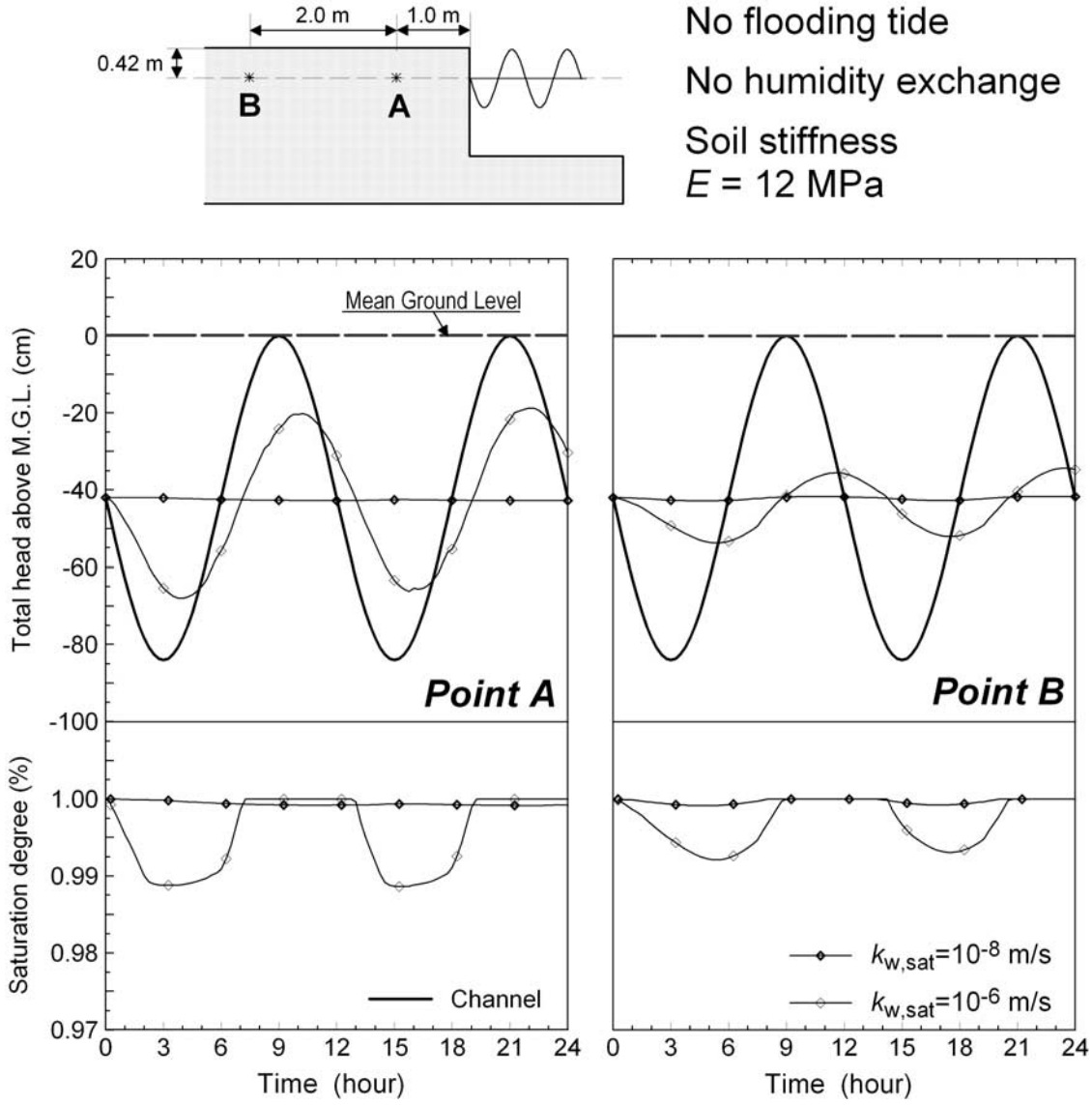

Figure 12. Total head and water saturation degree calculated in the analyses with different saturated water conductivity.

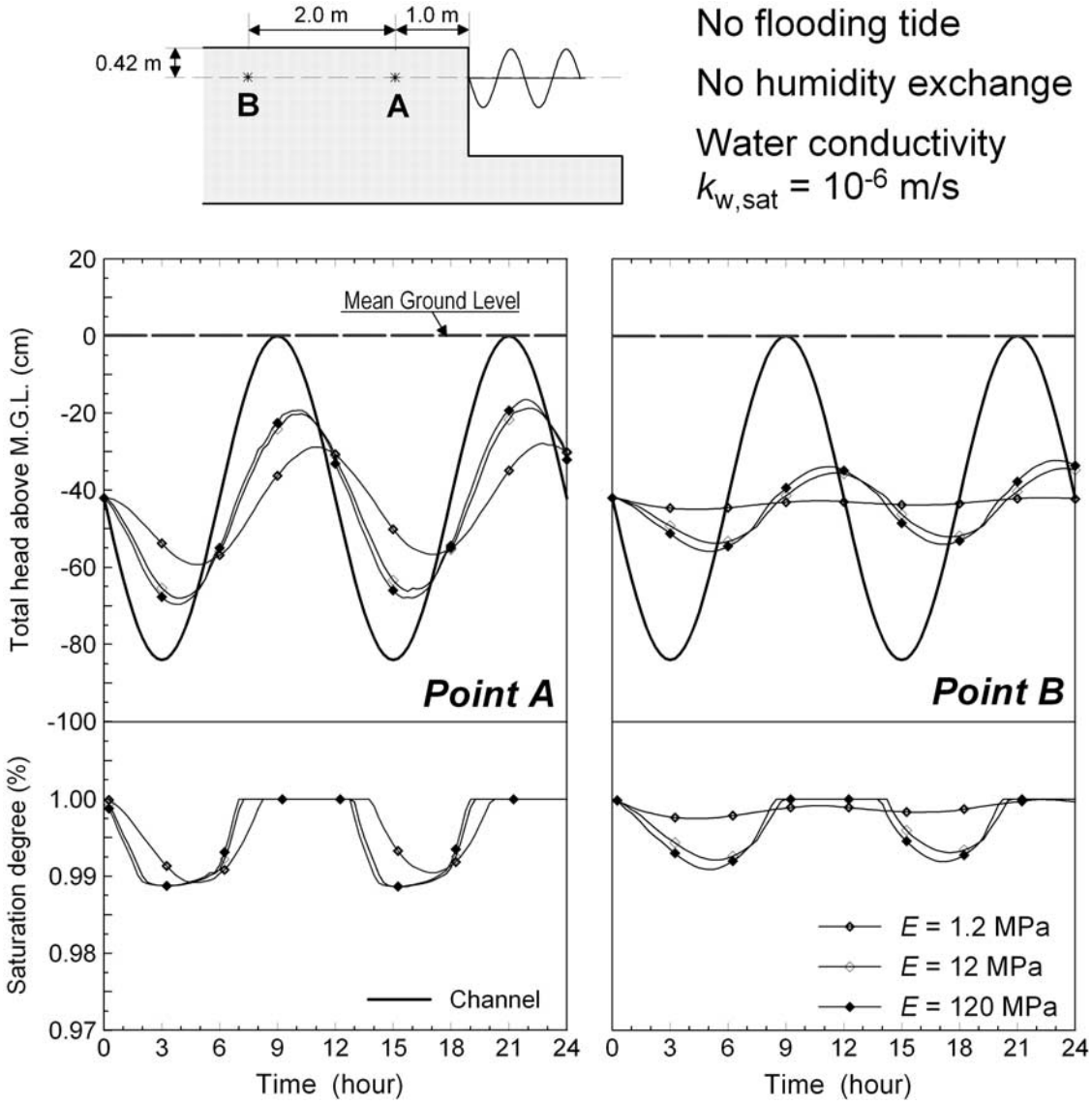

Figure 13. Total head and water saturation degree calculated in the analyses with different soil stiffness.

positive oscillations of channel water level, the marsh reaches full saturation also close to the ground surface.

7.2. Response Under Flooding

[69] Figure 14 shows the oscillation of groundwater table and saturation degree at points A and B in the case of marsh inundation, for both relevant stiffness $E = 1.2$ MPa and $E = 12.0$ MPa. In these analyses, no humidity exchange with the atmosphere is allowed to take place.

[70] Marsh inundation is marked by a sudden increase of water pressure at both points A and B, due to water infiltration from above which completely saturates the soil. The positive peak of the forcing cycle and related groundwater pressure are almost coincident in the case of higher stiffness, independently form the distance from the marsh border. On the contrary, a more deformable soil skeleton reduces the influence of submerging tide, thus giving a minor increase of water pressure in the ground.

[71] The associated oscillations of S_w, even though varying within a small range, are characterized by similar response, with the soil deformability acting as significant damping factor.

[72] After the peak, the groundwater pressure decay is marked by a completely different trend with respect to the case of increasing tide. In other words, under flooding tide, seepage from above recharges the ground, whereas, under descending tide the free water table in the marsh decreases at much slower rate. The permanence of a shallower water table is, again, strongly dependent on marsh ground deformability, which narrows the range of water pressure decay.

[73] Figure 15 depicts the trends of p^w and S_w over a longer period, in which a typical marsh inundation is followed by some days of nonsubmersion. The evolution of free water table along with the days after flooding displays, in absence of humidity exchange with atmosphere, a relevant rate of drainage and water outflow toward the channel, as effectively measured in the field. The discharging trend is clearly appreciable at point B, where, in the case of higher deformability, the groundwater oscillation

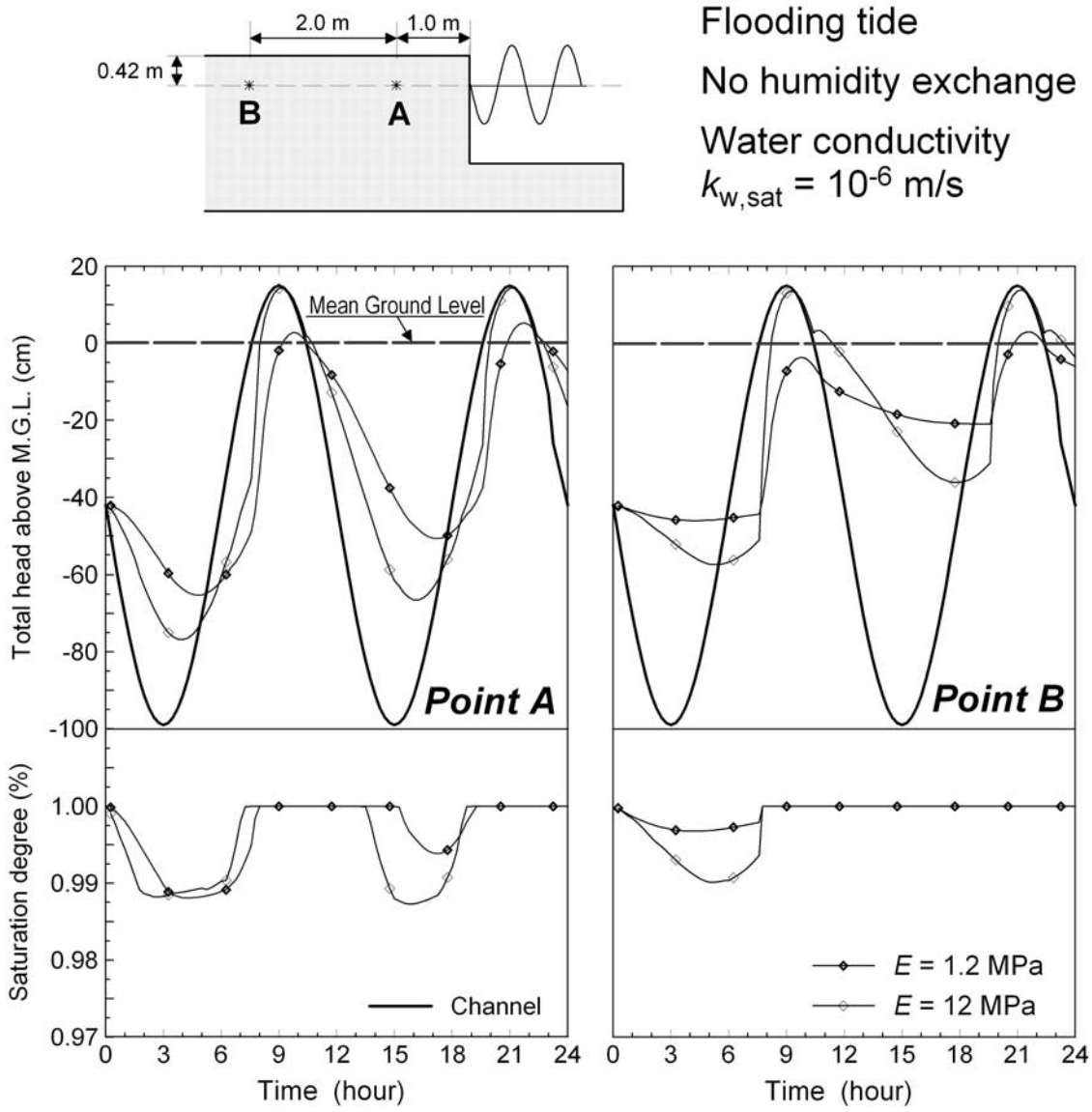

Figure 14. Total head and water saturation degree calculated in the analyses with marsh flooding.

almost vanishes. This is, of course, due to the more effective horizontal water outflow toward the nearby channel, which drains the groundwater from the inner zone of the marsh toward a steadily oscillating long-term condition (see Figure 12). Saturation degree at points A and B oscillates slightly in accordance to water table excursion.

[74] Keeping in mind the necessary simplifications used in modeling such a complex marsh soil behavior as far as the relevant boundary conditions, the results of these numerical analyses seem to match the basic features of the real groundwater oscillations, for the typical situation of flooding followed by some tidal cycles oscillating below the marsh surface.

7.3. Humidity Exchange With Atmosphere

[75] The above discussed situation rapidly changes when evapotranspiration is added as boundary condition to the marsh surface. Its effect can be clearly appreciated in Figure 16, at both points A and B. After flooding, the emptying of the marsh affected by the horizontal outflow toward the channel is dramatically increased by the evapotranspiration toward the atmosphere, leading to a water table below the assumed mean water level after 96 h. As far as the groundwater table deepens, the unsaturated zone rapidly increases, reaching also point B at larger distance form marsh border.

[76] The calculated water table excursion does not apparently seem in accordance with that observed on site, where the gradual decrease of groundwater pressure does not overcome the minimum tide oscillation. However, it must be noticed that the data shown in Figures 9 and 10 are referred to a seasonal period (i.e., early spring) in which a relatively high aerial humidity, coupled with a low Sun irradiation, features the Venice lagoon climate. For these reasons it seems that the water pressure evolution calculated in absence of significant evapotranspiration describes more properly the measured trends.

[77] However, based on suitable calibration of humidity exchange boundary condition along with the seasons of the year, the model could be used to predict water pressure and saturation degree in any period. For example, in the test here examined, the vertical water flow predicted by the

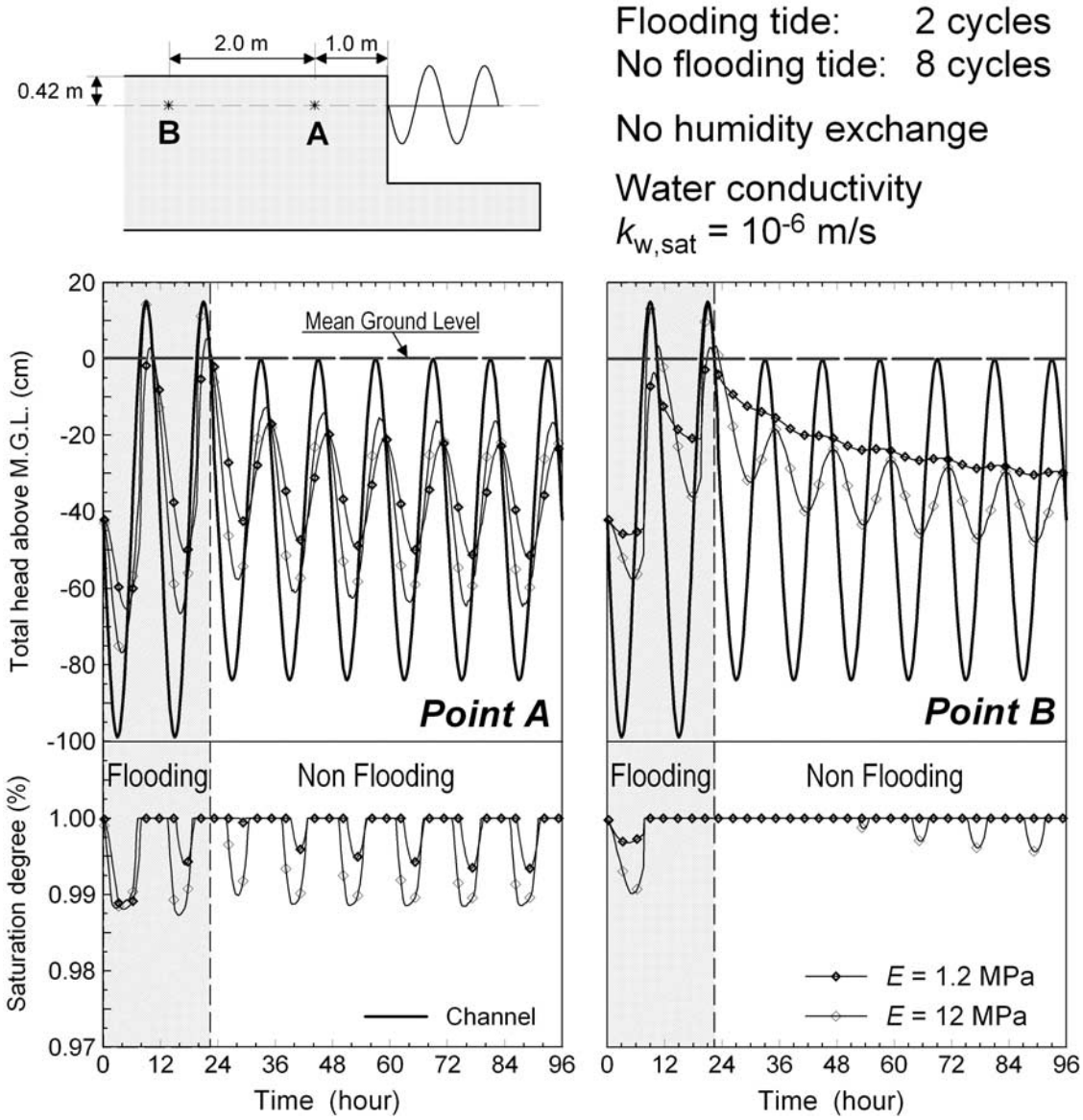

Figure 15. Total head and water saturation degree calculated along a 4-day period.

numerical model across the marsh surface turns out equal to about 4 mm/d, which may be a value characterizing an intense summer evapotranspiration on the salt marsh [*Dacey and Howes*, 1984].

8. Numerical Results: Stress Field

[78] It is important to analyze, in this context, the coupled response of the soil skeleton subjected to the groundwater and saturation oscillations discussed in section 7. This analysis may help in understanding the evolution of the stability of marsh scarp which tends, at long term, to collapse into the channel and then to be eroded by the stream. Marsh surface of the Venice lagoon has been consistently reduced in the last century leading to the execution of some interventions to protect the typical lagoon environment against dramatic erosion processes.

[79] To interpret stress state evolution under the forcing cycle, it is convenient to represent the induced stress field in terms of octahedral stresses, that is, the mean effective stress $\sigma'_m = -1/3(\boldsymbol{\sigma}':\mathbf{1})$ and the octahedral shear stress $\tau_{oct} = 1/3\sqrt{5(\boldsymbol{\sigma}':\mathbf{1}) - 3(\boldsymbol{\sigma}'^T:\boldsymbol{\sigma}')}$, because these scalar quantities (or similar) are invariants with respect to the reference system and, therefore, typically used to describe yield criteria for frictional materials.

[80] For the case of 96 h simulation with no humidity exchange, Figure 17 shows the trend of σ'_m and τ_{oct} (together with their ratio τ_{oct}/σ'_m) at two relevant points C and D, the first one located in the middle of the marsh scarp and the second at its base. Figure 17 (right) displays the mean effective stress oscillations against those of shear stress for the full period of simulation.

[81] The mean effective stress oscillates at both point C and D, being the major excursion at point C, whereas at point D no significant variation is observed. In addition, it may occur that σ'_m becomes occasionally negative at point C. On the contrary, higher shear stress oscillations are concentrated

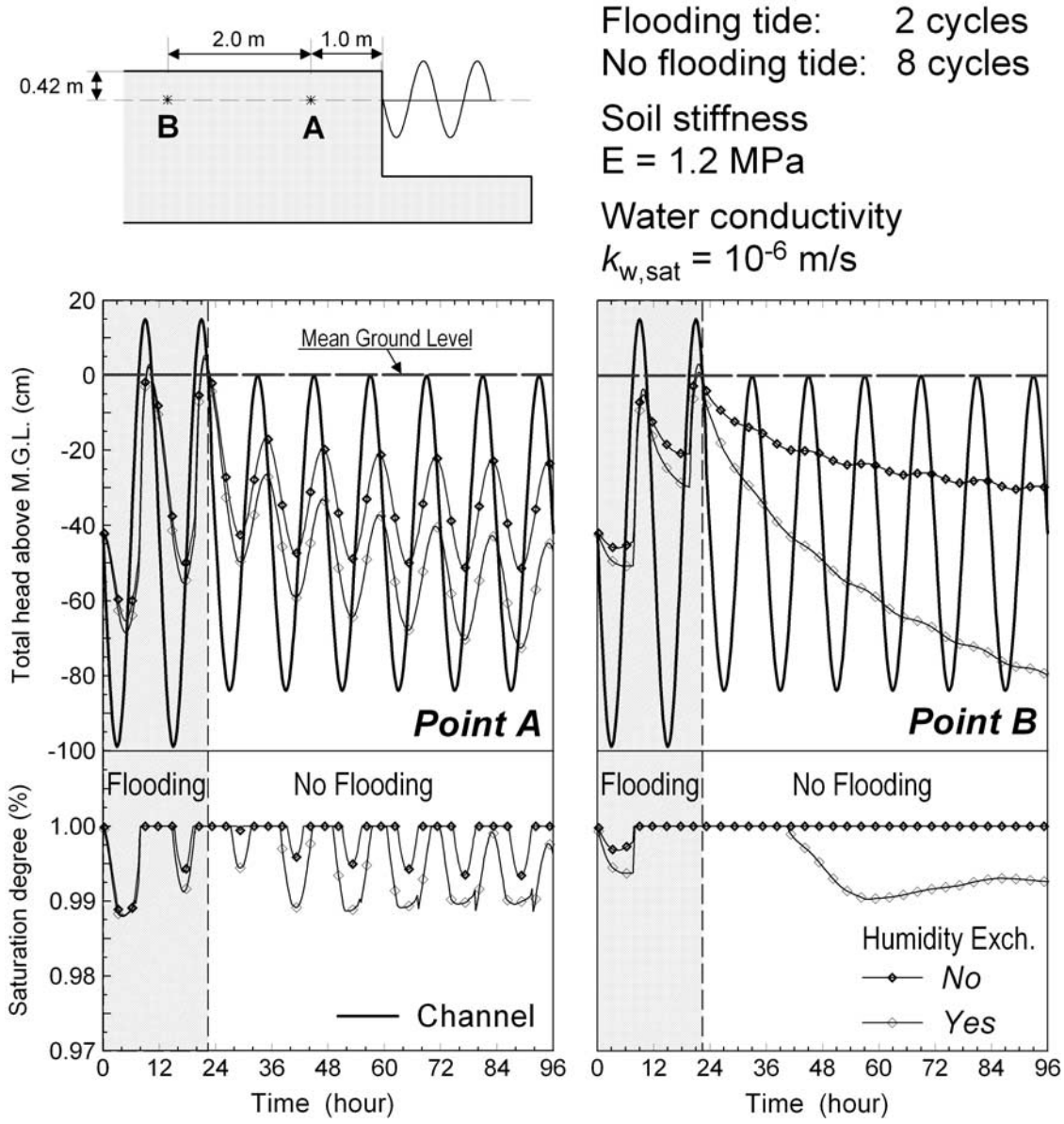

Figure 16. Effects of humidity exchange with atmosphere along a 4-day period.

at the base of the marsh scarp, where σ'_m is not particularly influenced by the variation of groundwater pressure.

[82] To guarantee the stability of the typical marsh slope (approaching the verticality) a cohesive strength component is, of course, required. It must be kept in mind that in Venice lagoon silts, whose major contribution to shear strength is due to friction, a weak cohesion may be ascribed to several different coexisting factors, such as capillary pressure in aerated zone, plant roots, very small cementation or diagenetic effects, which can easily vanish.

[83] Accumulation of shear and volumetric deformation induced by cyclic oscillation of shear and mean effective stresses may contribute to the decrease of cohesion, leading to a progressive failure that could propagate from the bottom of the scarp up to the tension crack observed in the shallower part of the marsh. Of course, to model this phenomenon it is necessary an elastoplastic analysis, that is planned as future research.

9. Conclusions

[84] A coupled THM analysis of Venice lagoon salt marshes has been studied by using a multiphase finite element approach, whose constitutive parameters have been selected on the basis of careful site and laboratory investigation.

[85] From the analyses carried out so far, the difficulty in modeling such a complex time-dependent boundary value problem was immediately evident, conditioned by many factors, among others the narrow amplitude of tidal oscillation, the very low effective stresses, the extremely small hydraulic gradients and effect of partial soil saturation. Nevertheless, the numerical approach adopted here seems capable of describing most of the relevant features

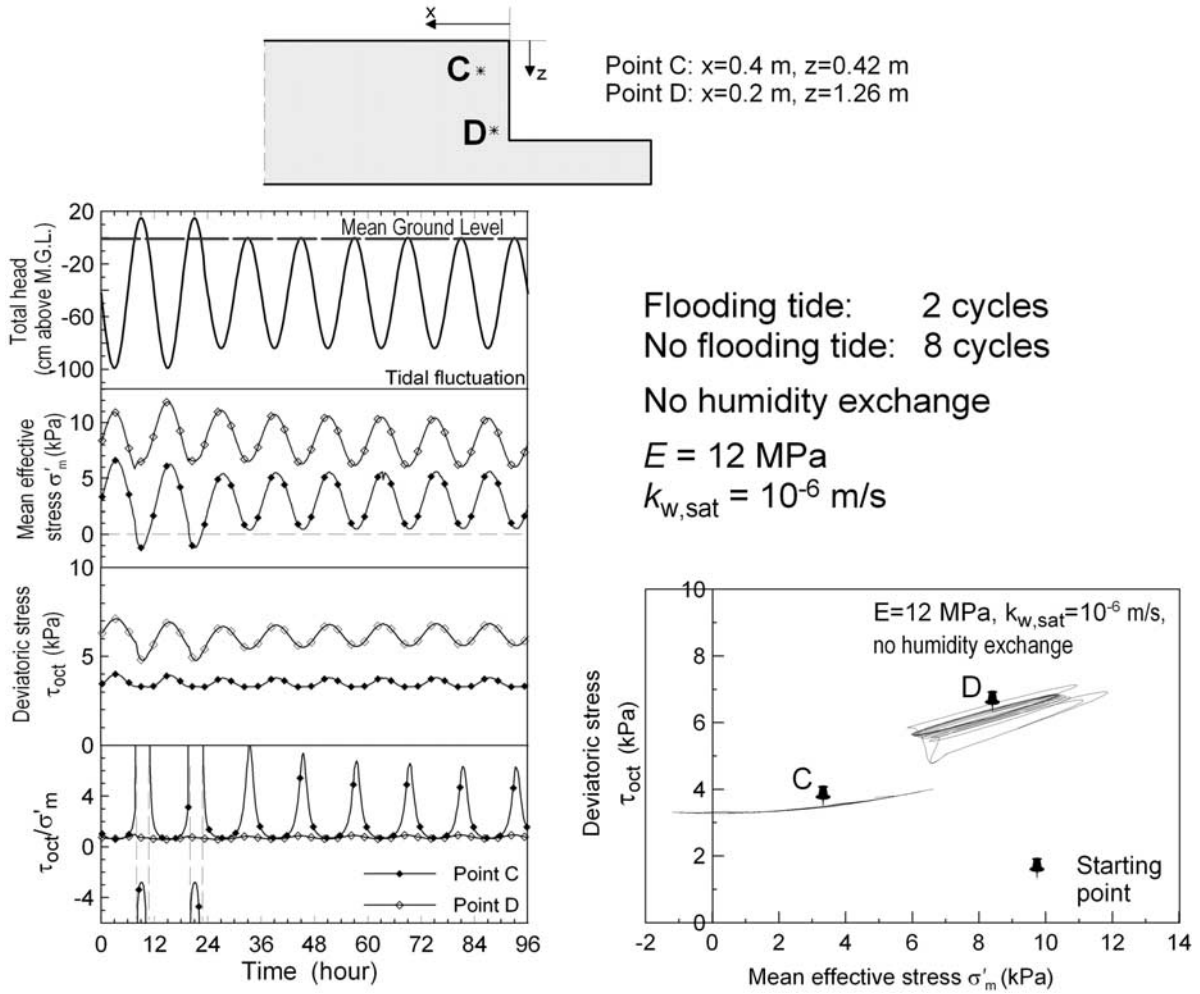

Figure 17. Stresses evolution near the marsh border during a 4-day-long period.

observed on site, thus showing the great importance of thermohydromechanical couplings to explain the groundwater pressure evolution induced by lagoon tide cycles.

[86] Despite the simplifications used in modeling the soil behavior, the results of the coupled numerical analyses seem to provide some interesting explanations concerning the evolving instability of marsh scarps, which is one of the main causes of the rapid overall deterioration of the typical Venice lagoon landscape.

[87] **Acknowledgments.** The authors would like to thank the University of Padua (research grants UNIPD 60A09-2037/07) and CORILA (the Consortium for Coordination of Research Activities Concerning the Venice Lagoon System) Venice, for the financial support.

References

Bianco, M., G. Bilardi, F. Pesavento, G. Pucci, and B. A. Schrefler (2003), A frontal solver tuned for fully coupled non-linear hygro-thermo-mechanical problems, *Int. J. Numer. Methods Eng.*, *57*, 1801–1818, doi:10.1002/nme.735.

Biot, M. A. (1941), General theory of three-dimensional consolidation, *J. Appl. Phys.*, *12*, 155–164, doi:10.1063/1.1712886.

Biscontin, G., S. Cola, J. M. Pestana, and P. Simonini (2007), Unified compression model for Venice lagoon natural silts, *J. Geotech. Geoenviron. Eng.*, *133*(8), 932–942.

Bishop, A. W., and G. E. Blight (1963), Some aspects of effective stress in saturated and partly saturated soils, *Geotechnique*, *13*, 177–197.

Borja, R. J. (2004), Cam-clay plasticity. Part V: A mathematical framework for three-phase deformation and strain localisation analyses of partially saturated porous media, *Comput. Methods Appl. Mech. Eng.*, *193*, 5301–5338, doi:10.1016/j.cma.2003.12.067.

Brooks, R. N., and A. T. Corey (1966), Properties of porous media affecting fluid flow, *J. Irrig. Drain. Div. Am. Soc. Civ. Eng.*, *92*(IR2), 61–68.

Butterfield, R., G. Gottardi, P. Simonini, and S. Cola (2003), A new interpretation of the compressibility of Venetian silty-clay soils, in *BGA International Conference on Foundations, Innovations, Observations, Design and Practice*, vol. 1, pp. 149–159, Thomas Telford, London.

Ceron, M. (2005), Comportamento idro-meccanico di un'argilla tenera essiccata e suo studio sperimentale, M.S. thesis, Univ. of Padova, Padua, Italy.

Cola, S., and P. Simonini (1999), Some remarks on the behavior of Venetian silts, in *2nd International Symposium on Pre-failure Behaviour of Geomaterials, IS Torino 99*, pp. 167–174, A. A. Balkema, Rotterdam, Netherlands.

Cola, S., and P. Simonini (2002), Mechanical behaviour of silty soils of the Venice lagoon as a function of their grading properties, *Can. Geotech. J.*, *39*(4), 879–893, doi:10.1139/t02-037.

Cola, S., L. Sanavia, and P. Simonini (2005), Modelling pore pressure response as a function of tide in the Venice lagoon marshes, in *Proceedings of the 11th International Conference on Computer Methods and Advances in Geomechanics*, edited by G. Barla and M. Barla, pp. 101–108, Pàtron Editore, Bologna, Italy.

Coussy, O. (2007), Revisiting the constitutive equations of unsaturated porous solids using a Langrangian saturation concept, *Int. J. Numer. Anal. Methods Geomech.*, *31*, 1675–1694, doi:10.1002/nag.613.

Dacey, J. W. H., and B. L. Howes (1984), Water uptake controls water table movement and sediment oxidation in short spartina marsh, *Science*, *224*, 487–489, doi:10.1126/science.224.4648.487.

Ehlers, W., T. Graf, and M. Ammann (2004), Deformation and localization analysis of partially saturated soil, *Comput. Methods Appl. Mech. Eng.*, *193*, 2885–2910, doi:10.1016/j.cma.2003.09.026.

Feola, A., E. Belluco, A. D'Alpaos, S. Lanzoni, M. Marani, and A. Rinaldo (2005), A geomorphic study of lagoonal landforms, *Water Resour. Res.*, *41*, W06019, doi:10.1029/2004WR003811.

Gawin, D., and L. Sanavia (2008), Modelling of cavitation in water saturated porous media considering effects of dissolved air, *Transp. Porous Media*, in press.

Gawin, D., and B. A. Schrefler (1996), Thermo- hydro- mechanical analysis of partially saturated porous materials, *Eng. Comput.*, *13*(7), 113–143, doi:10.1108/02644409610151584.

Gray, W. G., and S. M. Hassanizadeh (1991), Unsaturated flow theory including interfacial phenomena, *Water Resour. Res.*, *27*, 1855–1863, doi:10.1029/91WR01260.

Gray, W. G., and B. A. Schrefler (2001), Thermodynamic approach to effective stress in partially saturated porous media, *Eur. J. Mech. A Solids*, *20*, 521–538.

Hassanizadeh, M., and W. G. Gray (1979a), General conservation equations for multi-phase system: 1. Averaging technique, *Adv. Water Resour.*, *2*, 131–144, doi:10.1016/0309-1708(79)90025-3.

Hassanizadeh, M., and W. G. Gray (1979b), General conservation equations for multi-phase system: 2. Mass, momenta, energy and entropy equations, *Adv. Water Resour.*, *2*, 191–201, doi:10.1016/0309-1708(79)-6.

Hassanizadeh, M., and W. G. Gray (1980), General conservation equations for multi-phase system: 3. Constitutive theory for porous media flow, *Adv. Water Resour.*, *3*, 25–40, doi:10.1016/0309-1708(80)90016-0.

Hutter, K., L. Laloui, and L. Vulliet (1999), Thermodynamically based mixture models of saturated and unsaturated soils, *Mech. Cohes. Fric. Mater.*, *4*, 295–338, doi:10.1002/(SICI)1099-1484(199907)4:4 < 295:: AID-CFM64 > 3.0.CO;2-9.

Jiao, J. J., and Z. Tang (1999), An analytical solution of groundwater response to tidal fluctuation in a leaky confined aquifer, *Water Resour. Res.*, *35*, 747–752, doi:10.1029/1998WR900075.

Laloui, L., and C. Cekerevac (2003), Thermo-plasticity of clays: An isotropic yield mechanism, *Comput. Geotech.*, *30*, 649–660, doi:10.1016/j.compgeo.2003.09.001.

Laloui, L., C. Cekerevac, and B. François (2005), Constitutive modelling of the thermo-plastic behaviour of soils, *Rev. Eur. Genie Civ.*, *9*, 635–650.

Lewis, R. W., and B. A. Schrefler (1998), *The Finite Element Method in the Static and Dynamic Deformation and Consolidation of Porous Media*, John Wiley, Chichester, U.K.

Li, H., and J. J. Jiao (2002), Analytical solutions of tidal groundwater flow in coastal two-aquifer system, *Adv. Water Resour.*, *25*, 417–426, doi:10.1016/S0309-1708(02)00004-0.

Li, L., D. A. Barry, F. Stagnitti, and J. Y. Parlange (2000), Groundwater waves in a coastal aquifer: A new governing equation including vertical effects and capillarity, *Water Resour. Res.*, *36*, 411–420, doi:10.1029/1999WR900307.

Marani, M., S. Lanzoni, S. Silvestri, and A. Rinaldo (2004), Tidal landforms, patterns of halophytic vegetation and the fate of the lagoon of Venice, *J. Mar. Syst.*, *51*, 191–210, doi:10.1016/j.jmarsys.2004.05.012.

Marani, M., A. D'Alpaos, S. Lanzoni, L. Carniello, and A. Rinaldo (2007), Biologically controlled multiple equilibria of tidal landforms and the fate of the Venice lagoon, *Geophys. Res. Lett.*, *34*, L11402, doi:10.1029/2007GL030178.

Nuth, M., and L. Laloui (2008), Effective stress concept in unsaturated soils: Clarification and validation of a unified approach, *Int. J. Numer. Anal. Methods Geomech.*, *32*, 771–801, doi:10.1002/nag.645.

Rinaldo, A., S. Fagherazzi, S. Lanzoni, M. Marani, and W. E. Dietrich (1999a), Tidal networks: 2. Watershed delineation and comparative network morphology, *Water Resour. Res.*, *35*, 3905–3917, doi:10.1029/1999WR900237.

Rinaldo, A., S. Fagherazzi, S. Lanzoni, M. Marani, and W. E. Dietrich (1999b), Tidal networks: 3. Landscape-forming discharges and studies in empirical geomorphic relationships, *Water Resour. Res.*, *35*, 3919–3929, doi:10.1029/1999WR900238.

Romero, E., A. Gens, and A. Lloret (1999), Water permeability, water retention and microstructure of unsaturated compacted Boom clay, *Eng. Geol. Amsterdam*, *54*, 117–127, doi:10.1016/S0013-7952(99)00067-8.

Sanavia, L., B. A. Schrefler, and P. Steinmann (2002), A formulation for an unsaturated porous medium undergoing large inelastic strains, *Comput. Mech.*, *28*, 137–151, doi:10.1007/s00466-001-0277-8.

Sanavia, L., F. Pesavento, and B. A. Schrefler (2006), Finite element analysis of non-isothermal multiphase geomaterials with application to strain localization simulation, *Comput. Mech.*, *37*(4), 331–348, doi:10.1007/s00466-005-0673-6.

Sanavia, L., B. François, R. Bortolotto, L. Luison, and L. Laloui (2008), Finite element modelling of thermo-elasto-plastic water saturated porous materials, *J. Theoret. Appl. Mech.*, *38*, 7–24.

Schrefler, B. A. (1984), The finite element method in soil consolidation (with applications to surface subsidence), Ph.D. thesis, Univ. Coll. of Swansea, Swansea, U.K.

Schrefler, B. A. (2002), Mechanics and thermodynamics of saturated-unsaturated porous materials and quantitative solutions, *Appl. Mech. Rev.*, *55*(4), 351–388, doi:10.1115/1.1484107.

Simonini, P. (2004), Characterization of the Venice lagoon silts from in-situ tests and the performance of a test embankment, in *Proceedings of the ISC'02, Geotechnical and Geophysical Site Characterization*, vol. 1, pp. 187–207, Millpress, Rotterdam, Netherlands.

Simonini, P., and S. Cola (2002), Some pore pressure measurements at the marsh S. Felice in the Venice lagoon, paper presented at CORILA Workshop, Consortium for Coord. of Res. Activ. Concerning the Venice Lagoon Syst., Venice, Italy, 4–5 May.

Simonini, P., G. Ricceri, and S. Cola (2007), Geotechnical characterization and properties of Venice lagoon heterogeneous silts, in *Characterization and Engineering Properties of Natural Soils*, vol. 3, edited by T. S. Tan et al., pp. 2289–2331, Taylor and Francis, London.

Sun, H. (1997), A two-dimensional analytical solution of groundwater response to tidal loading in an estuary, *Water Resour. Res.*, *33*, 1429–1435, doi:10.1029/97WR00482.

Ursino, N., S. Silvestri, and M. Marani (2004), Subsurface flow and vegetation patterns in tidal environments, *Water Resour. Res.*, *40*, W05115, doi:10.1029/2003WR002702.

Zienkiewicz, O. C., A. Chan, M. Pastor, B. A. Schrefler, and T. Shiomi (1999), *Computational Geomechanics With Special Reference to Earthquake Engineering*, John Wiley, Chichester, U.K.

Zienkiewicz, O. C., and R. L. Taylor (2000a), *The Finite Element Method*, vol. 1, *The Basis*, Butterworth-Heinemann, Boston, Mass.

Zienkiewicz, O. C., and R. L. Taylor (2000b), *The Finite Element Method*, vol. 3, *Fluid Mechanics*, Butterworth-Heinemann, Boston, Mass.

S. Cola and P. Simonini, Department of IMAGE, via Ognissanti, University of Padova, I-35131 Padova PD, Italy. (simonetta.cola@unipd.it)

L. Sanavia and B. A. Schrefler, Department of Structural and Transportations Engineering, University of Padova, via F. Marzolo 9, I-35131 Padova PD, Italy.